Diffusive molecular dynamics simulations of lithiation of silicon nanopillars

J.P. Méndez, M. Ponga, M. Ortiz

PII: S0022-5096(17)30880-3
DOI: 10.1016/j.jmps.2018.03.008
Reference: MPS 3301

To appear in: *Journal of the Mechanics and Physics of Solids*

Received date: 30 September 2017
Revised date: 7 March 2018
Accepted date: 8 March 2018

Please cite this article as: J.P. Méndez, M. Ponga, M. Ortiz, Diffusive molecular dynamics simulations of lithiation of silicon nanopillars, *Journal of the Mechanics and Physics of Solids* (2018), doi: 10.1016/j.jmps.2018.03.008

Diffusive molecular dynamics simulations of lithiation of silicon nanopillars

J. P. Méndez[a], M. Ponga[b], M. Ortiz[a,*]

[a]*Division of Engineering and Applied Science, California Institute of Technology, Pasadena, CA 91125, USA.*
[b]*Department of Mechanical Engineering, The University of British Columbia, Vancouver, BC Canada V6T 1Z1, Canada*

Abstract

We report diffusive molecular dynamics simulations concerned with the lithiation of Si nano-pillars, i. e., nano-sized Si rods held at both ends by rigid supports. The duration of the lithiation process is of the order of miliseconds, well outside the range of molecular dynamics but readily accessible to diffusive molecular dynamics. The simulations predict an alloy $Li_{15}Si_4$ at the fully lithiated phase, exceedingly large and transient volume increments up to 300% due to the weakening of Si-Si iterations, a crystalline-to-amorphous-to-lithiation phase transition governed by interface kinetics, high misfit strains and residual stresses resulting in surface cracks and severe structural degradation in the form of extensive porosity, among other effects.

Keywords: Li-based batteries, Li diffusion, Lithiation, Non-equilibrium statistical mechanics, Long-term diffusion simulations, Diffusive molecular dynamics.

1. Introduction

Si nanowires have been investigated as building blocks for anode applications in high energy-density Li batteries, reaching theoretical specific capacities of up to 4212 mAh/g (Aifantis et al., 2010). However, Si nanowires are hampered by the mechanical degradation that occurs during lithiation, a fundamental process that takes place when Li cations enter the Si lattice

*Corresponding author
Email address: ortiz@caltech.edu (M. Ortiz)

during charging. Upon lithiation, Si loses its crystalline structure and the alloy becomes amorphous, with an attendant volume increase of approximately 300%. This volume increase, in turn, creates large internal stresses that induce plastic deformation, damage and fracture of the nanowire, leading to device failure after only a few charge cycles (Kasavajjula et al., 2007; Chan et al., 2008; Magasinski et al., 2010; Sethuraman et al., 2010). In order to mitigate these deleterious effects, a range of new battery designs are currently being assessed that employ nanowires and nanotubes (Chan et al., 2008; Deshpande et al., 2010; Choi et al., 2011), nanospheres (Yao et al., 2011), nanocomposites (Magasinski et al., 2010), thin films (Soni et al., 2011, 2012; Xiao et al., 2011), and other engineered materials. However, these efforts are hampered by imperfect understanding of key aspects of the Si lithiation process, such as the observed *brittle-to-ductile* transition and its role in nanowire degradation and cracking (Zhao et al., 2011), as well as the patterning that develops in thin film Si nanowires after a few charge/discharge cycles (Soni et al., 2011, 2012).

Si lithiation sets in motion a number of coupled atomic-level mechanisms, including mass transport, e. g., absorption and diffusion of Li, and phase transitions, including amorphization, swelling of Si and interface motion. The ability to accurately predict these processes quantitatively requires models affording fine resolution and fidelity on atomic scale. Simultaneously, the processes of interest, such as Si-based nanowire damage and degradation, occur on a device scale and over long times and after large numbers of operating cycles. Current approaches to modeling and simulation of Si lithiation are based on continuum theories (Bower et al., 2011; Ryu et al., 2011; Cui et al., 2012b), *ab-initio* atomistic methods (Zhao et al., 2011; Johari et al., 2011; Jung and Han, 2012) and molecular dynamics (MD) methods (Ostadhossein et al., 2015; Lee and Lee, 2014a; Wang et al., 2013). Continuum theories enable the simulation of device-scale samples and complete lithiation-delithiation processes, but are *a fortiori* empirical and interpolative in nature and require extensive calibration against integral test data, which detracts from their predictive ability. By way of contrast, conventional *ab-initio* or molecular dynamics methods are either parameter-free or calibrated based on fundamental device-independent properties. However, direct molecular dynamics requires the use of time steps of the order of the period of thermal vibration of the atoms and, therefore, is ill-suited to the study slow long-term phenomena. Likewise, Monte Carlo methods require the enumeration of transition paths and the elucidation of the corresponding

transition rates, which adds a level of empiricism on top of molecular dynamics and renders the approach intractable when the transition paths are numerous and complex.

These issues have motivated the development of modeling techniques capable of retaining full atomistic resolution while simultaneously enabling the simulation of long-term, diffusion mediated, non-equilibrium transport phenomena, including heat conduction (Kulkarni, 2006; Kulkarni et al., 2008; Ariza et al., 2011; Ponga et al., 2015, 2016) and mass transport (Venturini, 2011; Li et al., 2011; Sarkar et al., 2012; Venturini et al., 2014; Simpson et al., 2016). Following the terminology of Li et al. (2011), we will collectively refer to these techniques as Diffusive Molecular Dynamics (DMD). The essence of the approach is to describe the state of a system as a collection of *sites* that can be occupied or empty. A statistical-mechanical treatment of the ensemble then allows the sites to be partially occupied as well. The degree of occupancy of a site is measured by a local atomic molar fraction variable ranging from 0 (empty) to 1 (fully occupied). We specifically employ the non-equilibrium statistical mechanics framework developed by Kulkarni (2006); Kulkarni et al. (2008) and extended by Venturini (2011); Venturini et al. (2014). The evolution of the local atomic molar fraction variables is governed by an atomic-level kinetic equation akin to Ficks law and in the spirit of Onsager kinetics. The atomic-level kinetics is controlled by an empirical *master equation* that governs the evolution of the atomic molar fractions at each individual site (Li et al., 2011). The driving forces for this evolution derive from non-equilibrium atomic-level chemical potentials. These chemical potentials in turn follow directly from a free-entropy function, defined in terms of standard interatomic potentials, which generalizes the classical Helmholtz free energy to non-equilibrium conditions. Thus, the time evolution of the system may be viewed as the result of a competition between free-entropy maximization and atomic-level kinetics. The DMD framework has been successfully applied to thermo-mechanical dynamic problems (Kulkarni, 2006; Kulkarni et al., 2008; Ariza et al., 2011; Ponga et al., 2015, 2016, 2017), including heat conduction, and mass transport problems (Venturini, 2011; Venturini et al., 2014; Wang et al., 2015; Sun et al., 2017).

DMD is ideally suited to the study of Si lithiation by virtue of the slowness of the process, occurring on the diffusive time scale, and its atomistic nature. Conversely, Si lithiation sets forth an exacting test of any computational scheme by virtue of the complexity of the process, which involves long-term evolution and mass transport strongly coupled to large configura-

tional changes such as amorphization. The simulations reported in this work concern the lithiation of Si nano-pillars, i. e., nano-sized Si rods held at both ends by rigid supports. The duration of the lithiation process is of the order of miliseconds, well outside the range of MD but accessible to DMD. The simulations predict an alloy $Li_{15}Si_4$ at the fully lithiated phase, exceedingly large and transient volume increments up to 300% due to the weakening of Si-Si iterations, a crystalline-to-amorphous-to-lithiation phase transition governed by interface kinetics, high misfit strains and residual stresses resulting in surface cracks and severe structural degradation in the form of extensive porosity, among other effects. These predictions are in general overall agreement with experimental observations of silicon lithiation, which contributes to validating DMD and attests to its predictiveness.

2. Diffusive molecular dynamics

For completeness, we briefly summarize the relevant parts of theory as it bears on the present application (cf. Venturini et al. (2014) for a more general account).

2.1. Local equilibrium relations

We consider systems consisting of N *sites*, e. g., atoms or molecules, each of which can be of one of M species. For each site $i = 1, \ldots, N$, and each species $k = 1, \ldots, M$, we introduce the *occupancy function*

$$n_{ik} = \begin{cases} 1, & \text{if site } i \text{ is occupied by species } k, \\ 0, & \text{otherwise,} \end{cases} \tag{1}$$

in order to describe the *occupancy* of each site. We note that, from definition (1), we must have

$$\sum_{k=1}^{M} n_{ik} = 1 \tag{2}$$

at every site i. We shall denote by $\boldsymbol{n}_i = (n_{ik})_{k=1}^{M}$ the local occupancy array of site i. The *microscopic states* of the system are defined by the instantaneous position $\{\boldsymbol{q}\} = (\boldsymbol{q}_i)_{i=1}^{N}$, momenta $\{\boldsymbol{p}\} = (\boldsymbol{p}_i)_{i=1}^{N}$, and occupancy arrays $\{\boldsymbol{n}\} = (\boldsymbol{n}_i)_{i=1}^{N}$ of all N sites in the system. It follows from definition (1) that the occupancy functions $\boldsymbol{n}_i$ take values in a set, denoted $\mathcal{O}_M$, consisting of the

elements of $\{0,1\}^M$ that satisfy the constraint (2). In addition, the occupancy arrays $\{\boldsymbol{n}\}$ take values in the set

$$\mathcal{O}_{NM} = \{\{\boldsymbol{n}\},\ \boldsymbol{n}_i \in \mathcal{O}_M,\ i = 1, \ldots, N\}\ . \tag{3}$$

Within this ensemble, we assume that the statistics of the system obeys Jaynes' *principle of maximum entropy* (Jaynes, 1957a,b). This principle postulates that the probability density function $\rho(\{\boldsymbol{q}\}, \{\boldsymbol{p}\}, \{\boldsymbol{n}\})$, characterizing the probability of finding the system in a state $(\{\boldsymbol{q}\}, \{\boldsymbol{p}\}, \{\boldsymbol{n}\})$, maximizes the *information-theoretical entropy*

$$\mathcal{S}[\rho] = -k_B \langle \log \rho \rangle, \tag{4}$$

among all probability measures consistent with the constraints on the system. In (4) and subsequently, k_B denotes Bolzmann's constant. It is known from information theory that the *maximum-entropy*, or *max-ent* for short, probability density function is indeed the *least biased* probability density function consistent with the constraints on the system (Jaynes, 1957a,b).

In the present work, the processes under consideration are slow and the system may be assumed to be in thermal equilibrium. Under these conditions, an appropriate set of constraints is

$$\langle H \rangle = E, \tag{5a}$$

$$\langle n_{ik} \rangle = x_{ik}, \tag{5b}$$

$i = 1, \ldots, N$, $k = 1, \ldots, M$, where $H(\{\boldsymbol{q}\}, \{\boldsymbol{p}\})$ is the Hamiltonian of the system, E is its total energy and x_{ik} is the atomic molar fraction of species k at site i. We note that, by virtue of (2), the local atomic molar fractions satisfy the identities

$$\sum_{k=1}^{M} x_{ik} = 1, \qquad i = 1, \ldots, N. \tag{6}$$

Thus, x_{ik} may be interpreted as the expectation that site i be occupied by a particle of species k.

Enforcing the constraints (5) by means of Lagrange multipliers $k_B\beta$ and $k_B\{\boldsymbol{\gamma}\} \equiv (k_B\boldsymbol{\gamma}_i)_{i=1}^N$, with $\boldsymbol{\gamma}_i = (\gamma_{ik})_{k=1}^M$, gives, after a straightforward calculation,

$$\rho = \frac{1}{\Xi(\beta, \{\boldsymbol{\gamma}\})} \mathrm{e}^{-\beta H(\{\boldsymbol{q}\},\{\boldsymbol{p}\}) + \{\boldsymbol{\gamma}\}^T\{\boldsymbol{n}\}}, \tag{7}$$

where

$$\Xi = \sum_{\{\boldsymbol{n}\}\in\mathcal{O}_{NM}} \int \mathrm{e}^{-\beta H(\{\boldsymbol{q}\},\{\boldsymbol{p}\})+\{\boldsymbol{\gamma}\}^T\{\boldsymbol{n}\}}\, dq\, dp, \tag{8}$$

and, in view of (6), we append the restrictions

$$\sum_{k=1}^{M} \gamma_{ik} = 0 \tag{9}$$

in order to render $\{\boldsymbol{\gamma}\}$ determinate. By analogy to equilibrium statistical mechanics, we may interpret Eqs. 7 and 8 as non-equilibrium generalizations of the Gibbs grand-canonical probability density function and the grand-canonical partition function, respectively. Similarly, we interpret

$$T = \frac{1}{k_B\beta}, \tag{10}$$

as the absolute temperature of the system, and

$$\boldsymbol{\mu}_i = \frac{\boldsymbol{\gamma}_i}{\beta} = k_B T \boldsymbol{\gamma}_i \tag{11}$$

as the *site chemical-potential array* of site i, respectively. However, we note that, unlike equilibrium statistical mechanics, the site chemical-potentials need not be uniform and may vary from site to site when the system is away from equilibrium.

The *total physical entropy* S may be identified with the information entropy at the grand-canonical distribution, namely,

$$S = k_B\beta\langle H\rangle - k_B\{\boldsymbol{\gamma}\}^T\{\langle\boldsymbol{n}\rangle\} + k_B \log\Xi(\beta,\{\boldsymbol{\gamma}\}). \tag{12}$$

A straightforward calculation gives the *equilibrium relations* as

$$\beta = \frac{1}{k_B}\frac{\partial S}{\partial E}(E,\{\boldsymbol{x}\}), \tag{13a}$$

$$\gamma_{ik} = -\frac{1}{k_B}\frac{\partial S}{\partial x_{ik}}(E,\{\boldsymbol{x}\}), \tag{13b}$$

which relate the energy and site atomic molar fractions to the temperatures and site chemical potentials. Under isothermal conditions, it is convenient to work with the grand-canonical free entropy Φ

$$\Phi = k_B \log\Xi(\beta,\{\boldsymbol{\gamma}\}), \tag{14}$$

with the properties

$$E = -\frac{1}{k_B}\frac{\partial \Phi}{\partial \beta}(\beta, \{\boldsymbol{\gamma}\}), \tag{15a}$$

$$x_{ik} = \frac{1}{k_B}\frac{\partial \Phi}{\partial \gamma_{ik}}(\beta, \{\boldsymbol{\gamma}\}), \tag{15b}$$

which effectively invert the equilibrium relations (13).

2.2. Meanfield approximation

In general, the calculation of the entropy in closed form as detailed in the previous section is generally intractable due to the highly coupled partition function of the system. This raises the need to use an approximation theory. Venturini et al. (2014) have extended the classical variational mean field theory (Yeomans, 1992) to systems away from equilibrium. The resulting variational framework provides a convenient basis for the formulation of computationally tractable models. Within this approximation, we consider classes of parameterized *trial Hamiltonians* $H_0(\{\boldsymbol{q}\}, \{\boldsymbol{p}\})$ and the corresponding grand-canonical distributions

$$\rho_0 = \frac{1}{\Xi_0} \mathrm{e}^{-\beta H_0(\{\boldsymbol{q}\},\{\boldsymbol{p}\}) + \{\boldsymbol{\gamma}\}^T \{\boldsymbol{n}\}}, \tag{16}$$

and grand-canonical partition functions

$$\Xi_0 = \sum_{\{\boldsymbol{n}\} \in \mathcal{O}_N} \int \mathrm{e}^{-\beta H_0(\{\boldsymbol{q}\},\{\boldsymbol{p}\}) + \{\boldsymbol{\gamma}\}^T \{\boldsymbol{n}\}} \, dq \, dp. \tag{17}$$

For every trial Hamiltonian, the free-entropy inequality

$$\Phi \geq k_B \log \Xi_0(\beta, \{\boldsymbol{\gamma}\}) - k_B \beta \langle H - H_0 \rangle_0 \equiv \mathcal{F}[H_0], \tag{18}$$

with the equality attained for $H_0 = H$. Thus, the best trial Hamiltonian is that which maximizes the Bogoliubov functional $\mathcal{F}[H_0]$ within the class of trial Hamiltonians under consideration.

The applications of interest here involve processes that take place on a diffusive time scale and for which inertia effects are negligible. We therefore restrict all phase integrals to the subspace $\{\boldsymbol{p}\} = \{\boldsymbol{0}\}$ and consider trial

potentials of the simple form (cf. Kulkarni (2006); Kulkarni et al. (2008); Venturini (2011); Venturini et al. (2014))

$$V_0(\{\boldsymbol{q}\}) = \sum_{i=1}^{N} \frac{k_i}{2} |\boldsymbol{q}_i - \bar{\boldsymbol{q}}_i|^2, \tag{19}$$

where $\{k\} = (k_i)_{i=1}^N$ is a collection of spring constants, to be determined variationally. For this particular mean field model, the mean field grand-canonical partition function (17) evaluates to

$$\begin{aligned} \Xi_0 &= \sum_{\{n\} \in \mathcal{O}_N} \int \mathrm{e}^{-\beta V_0(\{\boldsymbol{q}\}) + \{\boldsymbol{\gamma}\}^T \{\boldsymbol{n}\}} \, dq \\ &= \prod_{i=1}^{N} \Big(\frac{2\pi}{\beta k_i} \Big)^{3/2} \sum_{k=1}^{M} \mathrm{e}^{\gamma_{ik}}, \end{aligned} \tag{20}$$

the grand-canonical distribution function (16) to

$$\rho_0 = \frac{1}{\Xi_0(\beta, \{\boldsymbol{\gamma}\})} \mathrm{e}^{-\beta V_0(\{\boldsymbol{q}\}) + \{\boldsymbol{\gamma}\}^T \{\boldsymbol{n}\}}, \tag{21}$$

and the Bogoliubov functional (18) to

$$\begin{aligned} \mathcal{F} = 3k_B \sum_{i=1}^{N} \log \Big(\frac{2\pi}{\beta k_i} \Big) + k_B \sum_{i=1}^{N} \log \sum_{k=1}^{M} \mathrm{e}^{\gamma_{ik}} \\ + \frac{3k_B}{2} N - k_B \beta \langle V \rangle_0. \end{aligned} \tag{22}$$

Differentiating, we obtain

$$-\frac{1}{k_B} \frac{\partial \mathcal{F}}{\partial \bar{\boldsymbol{q}}_i} = \beta \langle \frac{\partial V}{\partial \boldsymbol{q}_i} \rangle_0 = \boldsymbol{0}, \tag{23a}$$

$$-\frac{1}{k_B} \frac{\partial \mathcal{F}}{\partial k_i} = \beta \frac{\partial}{\partial k_i} \langle V \rangle_0 + \frac{3}{2k_i} = 0, \tag{23b}$$

$$x_{ik} = \frac{1}{k_B} \frac{\partial \mathcal{F}}{\partial \gamma_{ik}} = \frac{\mathrm{e}^{\gamma_{ik}}}{\sum_{l=1}^{M} \mathrm{e}^{\gamma_{il}}}, \tag{23c}$$

which gives the effective mechanical equilibrium equations, mean field optimality condition and chemical equilibrium equations, respectively.

2.3. Calculation of the mean field phase averages

We note that the mean field phase averages $\langle \cdot \rangle_0$ in (23) entail integration against the Gaussian function (21). Such integrals can be conveniently computed numerically using Gaussian quadrature (Kulkarni, 2006; Kulkarni et al., 2008). In the present work, all mean field phase averages are computed using third-order Gaussian-quadrature rules (Stroud, 1971). The calculation of phase averages additional entails sums over all the possible occupancy states of the system. These sums are of combinatorial complexity and their exact evaluation is computationally costly (cf. Gonzalez-Ferreiro et al. (2016) for Monte Carlo summation schemes). Following Venturini et al. (2014), we approximate the sums by means of Jensen's inequality and write

$$\begin{aligned} \langle V \rangle_0 &= \frac{1}{\Xi_0} \sum_{\{n\} \in \mathcal{O}_N} \int V(\{\boldsymbol{q}\}, \{\boldsymbol{n}\}) \mathrm{e}^{-\beta V_0(\{\boldsymbol{q}\}) + \{\boldsymbol{\gamma}\}^T \{\boldsymbol{n}\}} \, dq \\ &\approx \frac{1}{\Xi_0} \int V(\{\boldsymbol{q}\}, \{\boldsymbol{x}\}) \mathrm{e}^{-\beta V_0(\{\boldsymbol{q}\}) + \{\boldsymbol{\gamma}\}^T \{\boldsymbol{x}\}} \, dq. \end{aligned} \tag{24}$$

We recall that Jensen's inequality supplies an upper bound for averages of convex functions. The combination of mean field approximation, Gaussian quadrature and Jensen's inequality finally enables the efficient 'on-the-fly' calculation of phase averages and renders the approach computable.

2.4. Kinetic relations for mass transport

We note that the system of equations (23) is not closed and, in order to close the system, *kinetic equations* for the evolution of the atomic molar fractions need to be appended. The general structure of these equations can be elucidated as follows. We begin by noting the the mass flow into site i may be expressed in conservation form as

$$\dot{\boldsymbol{x}}_i = \sum_{j \neq i} \boldsymbol{J}_{ij}, \tag{25}$$

where $\boldsymbol{J}_{ij} = -\boldsymbol{J}_{ji}$ is the discrete mass flux array from site j to i.

Additionally, a straightforward calculation shows that

$$\Sigma_{ij} = \boldsymbol{K}_{ij}^T \boldsymbol{J}_{ij} \geq 0, \tag{26}$$

with

$$\boldsymbol{K}_{ij} = \frac{1}{T}(\boldsymbol{\mu}_i - \boldsymbol{\mu}_j) = k_B(\boldsymbol{\gamma}_i - \boldsymbol{\gamma}_j) \ , \tag{27}$$

measures the *internal entropy production rate* for the site pairs, i. e., the entropy rate within the pair in excess of the entropy rate due to the external supply of mass. The structure of (26) identifies as $\boldsymbol{K}_{ij}$ as the driving force for the fluxes $\boldsymbol{J}_{ij}$. Following Onsager, we postulate kinetic laws of the general form

$$\boldsymbol{J}_{ij} = -\frac{\partial \psi}{\partial \boldsymbol{K}_{ij}}(\{\boldsymbol{K}\}), \tag{28}$$

where ψ is a discrete kinetic potential, to be modelled. We may regard (28) as a *discrete Fick law* of diffusion.

3. A model for the Si-Li system

The general framework just outlined requires two system-specific inputs: i) An interatomic potential V, and ii) a discrete kinetic potential ψ. We emphasize that both the interatomic force field and the kinetic relations are regarded as *empirical* relations and, as such, subject to modeling. We proceed to enumerate the specific modeling choices for the Si-Li system under consideration in this work.

3.1. Atomic structure

We consider systems consisting of Si atoms, initially arranged in a diamond structure, and Li atoms at sites initially coincident with the interstitial sites of the Si diamond lattice. We specifically consider: hexagonal interstitials (1 interstitial per Si atom); tetrahedral interstitials (2 interstitials per Si atom) and bond-centered interstitials (2 interstitials per Si atom) (Needs, 1999; Pichler, 2004). By this choice of interstitials, there can be a maximum of 5 Li atoms per Si atom. This type of coverage suffices to account for the lithiated phase of Si at equilibrium, which is measured at 3.75 Li atoms per Si atom (Obrovac and Christensen, 2004; Hatchard and Dahn, 2004).

As a further simplification, we designate the sites of the system as either Si or Li sites. We use index sets I_{Si} and I_{Li} to index the Si and Li sites, respectively. By this assumption, the state of the system can be described by means of a single occupancy variable n_i per site. In particular, if i is a Si site, $i \in I_{\mathrm{Si}}$, (respectively, a Li site, $i \in I_{\mathrm{Li}}$), then $n_i = 0$ if the site is empty and $n_i = 1$ if the site is occupied. In terms of the more general framework outlined in the Section 2.1, this particular choice corresponds to setting: $n_{i,Si} = n_i$, $n_{i,Li} = 0$ if $i \in I_{\mathrm{Si}}$; and $n_{i,Li} = n_i$, $n_{i,Si} = 0$ if $i \in I_{\mathrm{Li}}$. Likewise, the corresponding atomic molar fractions have the structure : $x_{i,Si} = x_i$,

$x_{i,Li} = 0$ if $i \in I_{\mathrm{Si}}$; and $x_{i,Li} = x_i$, $x_{i,Si} = 0$ if $i \in I_{\mathrm{Li}}$. In particular, the state of the system is characterized by a single atomic molar fraction x_i per site.

3.2. Si-Li interatomic potential

In calculations, we employ the second Nearest Neighbor Modified Embedded-Atom Method potential (2NN-MEAM) of Cui *et al.* (Cui et al., 2012a). The structure of the potential is

$$V = \sum_{i=1}^{N} \Big[n_i F_i(\overline{\rho}_i) + \frac{1}{2} \sum_{j \neq i} n_i n_j S_{ij} \phi_{ij}(r_{ij}) \Big], \tag{29}$$

where $F_i(\overline{\rho}_i)$ is the energy of embedding site i in the local electron density $\overline{\rho}_i$, ϕ_{ij} is a pairwise interaction between sites i and j, $r_{ij} = |\boldsymbol{q}_j - \boldsymbol{q}_i|$, S_{ij} is a many-body screening factor between sites i and j due to all other neighbor sites k, and n_i and n_j are the atomic occupancies of the sites i and j, respectively. The electron density $\overline{\rho}_i$ is composed of a spherically symmetric partial electron density, $\rho_i^{(0)}$, and angular contributions, $\rho_i^{(1)}$, $\rho_i^{(2)}$ and $\rho_i^{(3)}$. These partial electron densities depend on the surrounding atomic sites and the atomic electron density as

$$\rho_j^{a(h)}(r_{ij}) = n_j \rho_0 \exp[-\beta^{(h)}(\frac{r_{ij}}{r_e} - 1)] \tag{30}$$

where ρ_0 is a scaling factor, $\beta^{(h)}$ are adjustable parameters and r_e is the nearest-neighbor distance in the reference structure at equilibrium. The screening factor is

$$S_{ij} = \prod_{k \neq i,j} S_{ikj}(n_k), \tag{31}$$

where S_{ikj} is the screening of sites i and j by site k. Specifically, we take

$$S_{ikj} = f\left(\frac{C_{ikj} - C_{min,ikj}}{C_{max,ikj} - C_{min,ikj}} \right) n_k + (1 - n_k), \tag{32}$$

where $C_{min,ikj}$ and $C_{max,ikj}$ are parameters that depend on the $i-k-j$ triplet type,

$$C_{ikj} = 1 + 2\frac{r_{ij}^2 r_{ik}^2 + r_{ij}^2 r_{jk}^2 - r_{ij}^4}{r_{ij}^4 - (r_{ik}^2 - r_{jk}^2)^2,} \tag{33}$$

and

$$f(x) = \begin{cases} 1 & x \geq 1, \\ [1-(1-x)^4]^2 & 0 < x < 1, \\ 0 & x \leq 0. \end{cases} \tag{34}$$

is a cutoff function. Further details of the potential and values of the constants for the Si-Li system can be found in the original publication (Cui et al., 2012a).

3.3. Kinetics of Li diffusion

Following Zhang and Curtin (2008) and Li et al. (2011), we assume that mass transport is governed by the master equation

$$\frac{\partial x_i}{\partial t} = \sum_{\langle i,j \rangle} \nu \mathrm{e}^{-\beta E_b} \Big(x_j(1-x_i)\mathrm{e}^{\beta(\mu_j-\mu_i)/2} - x_i(1-x_j)\mathrm{e}^{\beta(\mu_i-\mu_j)/2} \Big), \tag{35}$$

where the sum runs over all connected neighbors, ν is the hoping frequency, E_b is a barrier energy, and the chemical potentials follow from (9), (11) and (23c), which under the present assumptions specializes to

$$x_i = \frac{\mathrm{e}^{\beta\mu_i}}{\mathrm{e}^{\beta\mu_i} + \mathrm{e}^{-\beta\mu_i}}, \tag{36}$$

or, in inverse form,

$$\mu_i = \frac{k_B T}{2} \log \frac{x_i}{1-x_i}. \tag{37}$$

A key aspect of the master equation used to simulate diffusion is that the effective transport rate depends on the activation energy E_b and, simultaneously, on the local chemical potentials of the lattice sites as derived from the free-entropy function. While the activation energy E_b is taken to be constant, the local chemical potentials depend on the local environment, with the result that diffusion is strongly coupled to the evolution of the lattice sites.

A longwave analysis (cf., e. g., Venturini et al. (2014); Tritsaris et al. (2012)) gives the relation

$$D \sim d^2 \nu \mathrm{e}^{-\beta E_b}, \tag{38}$$

where D is the macroscopic diffusion coefficient and d is an interatomic distance. This relation can be used to calibrate the kinetic model in terms of measured experimental data. However, there are wide disparities in the reported values of the diffusion coefficient D, with values randing from 10^{-9}cm $^2/s$ to 10^{-14} cm$^2/s$ (Ruffo et al., 2009; Xie et al., 2010; Yoshimura et al., 2007; Ding et al., 2009). In addition, the diffusion coefficient is Li-concentration dependent (Ding et al., 2009) and differs markedly between the crystalline or amorphous Si. Similarly, but at the atomistic scale, there are wide disparities in hoping frequency and barrier energy values depending on the local environment of the Li atoms. Thus, Tritsaris et al. (2012) predicted an energy barrier of 0.55 eV for hops between tetrahedral interstitials sites in crystalline Si and energy barriers ranging from 0.1 eV to 2.4 eV in amorphous Si. Kuhn et al. (2011) found an activation energy of 0.18 eV for 1D diffusion and of $0.32 - 0.55$ eV for 3D diffusion in $Li_{12}Si_7$ alloys; Yan et al. (2015) reports an energy barrier of 0.5 eV for hops between two tetrahedral interstitials sites; and Dunst et al. (2015) found that the average activation energy for long-range Li transport may as high as 0.65 eV in amorphous Si.

In calculations, we assume a value of $\nu = 10^{13}$ s^{-1} for the hopping frequency at $T = 300$ K and an energy barrier of $E_b = 0.441$ eV, corresponding to a Li diffusion coefficient of 10^{-12} cm^2/s in the ballpark of experimental observation (Ruffo et al., 2009; Xie et al., 2010; Yoshimura et al., 2007; Ding et al., 2009). We note that, in real materials, the parameters ν and E_b vary as a function of the local atomic environment, which adds complexity to the lithiation process (Haftbaradaran et al., 2011). This added complexity notwithstanding, the validation tests presented in the sequel suggest that averaged and constant values may be used to a good approximation.

3.4. Verification and validation tests

We have assessed the accuracy of the equilibrium properties predicted by the max-ent formalism with the aid of several test cases. Fig. 1 shows the energy per atom as a function of volume at 300K of bcc Li, diamond Si and L12 Li-Si as computed from max-ent and from direct MD calculations using LAMMPS (Plimpton, 1995). As may be seen from the figure, the agreement is excellent and is suggestive of a high degree of accuracy in the way in which max-ent accounts for thermal effects. For the same three crystal structures, Fig. 2 compares the dependence of the thermal expansion coefficient on temperature obtained from max-ent using the 2NN-MEAM potential (Cui et al., 2012a) with previous MD results (Lee, 2007) and experimental measurements

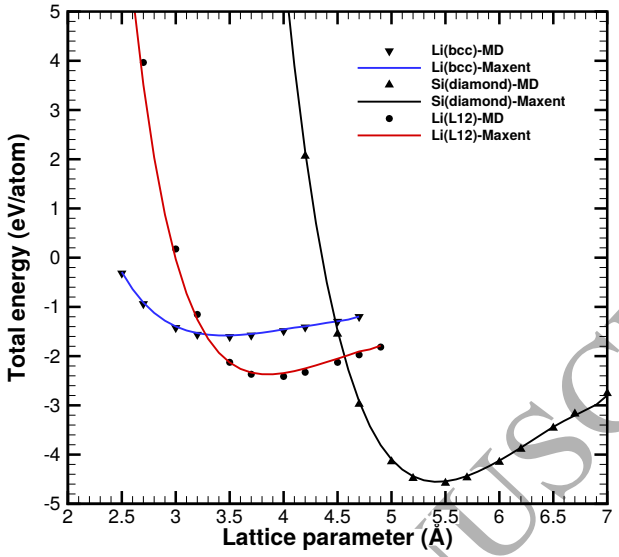

Figure 1: Comparison of the total energy versus the lattice parameter between MD and Maxent at 300K for several crystals: Li(BCC structure), Si(diamond structure) and a Si-Li alloy(L12 structure).

(Touloukian et al., 1975; Yim and Paff, 1974; Anderson and Swenson, 1985). As may be seen from the figure, the overall trends are well-captured by max-ent, which again reinforces confidence in the ability of the max-ent formalism to predict equilibrium properties over a range of temperatures.

As an additional test, we have computed the energies of a vacancy and a Li tetrahedral-type interstitial in Si at 300K and compared them against values from molecular statics, including the effect of the temperature given by the equipartition of the kinetic energy as $(3/2)Nk_BT$. Table 1 shows the respective formation energies for the single vacancy and the tetrahedral interstitial. The agreement between methods is noteworthy. The computed energies are also in agreement with other works (Lee et al., 1998; Needs, 1999; Leung et al., 1999) and in the ballpark of force-field methods.

4. Silicon nanopillar lithiation

We apply the preceding DMD framework to the study of lithiation of Si nanopillars.

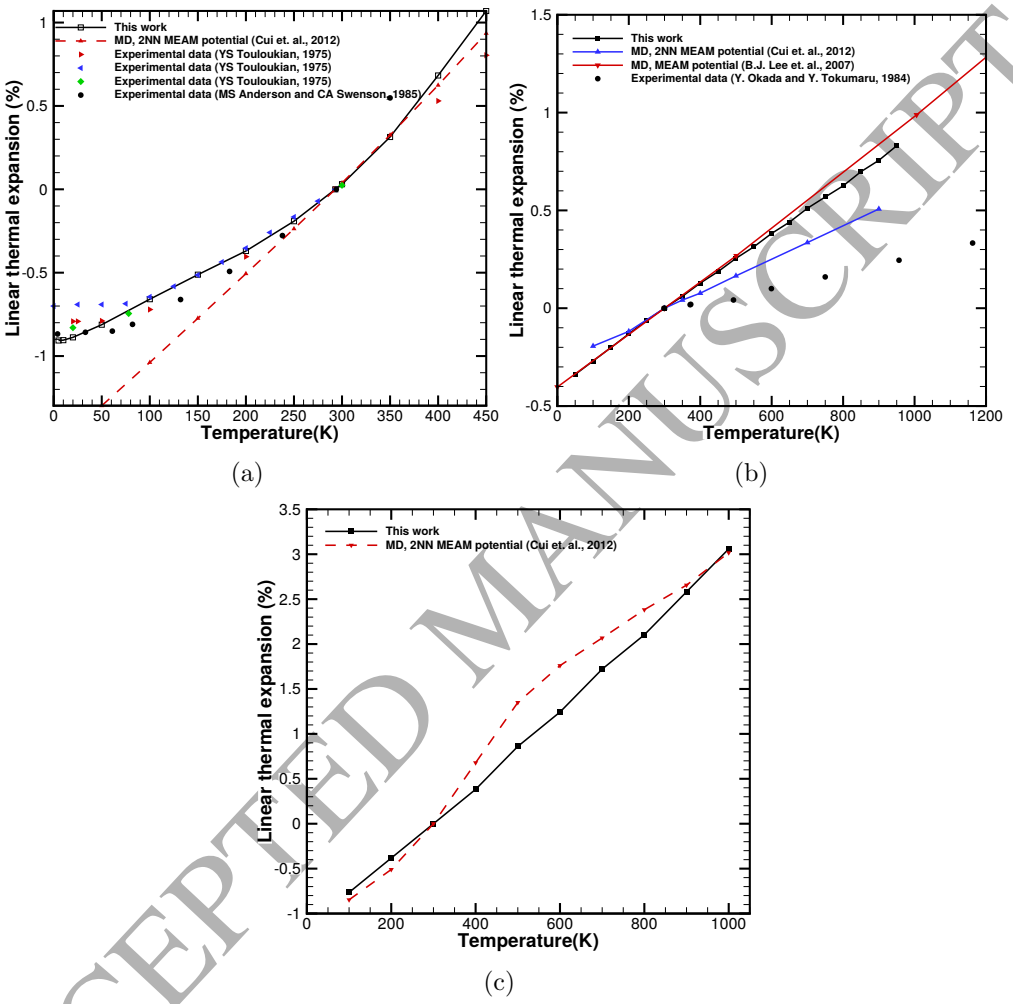

Figure 2: Thermal expansion for (a) Li (BBC structure), (b) Si (diamond structure), and (c) Li and Si alloy (L12 structure). The computed curves are compared against experimental values (Touloukian et al., 1975; Yim and Paff, 1974; Anderson and Swenson, 1985) and previous MD results (Lee, 2007).

Table 1: Comparison of formation energies for a single vacancy and a Li tetrahedral interstitial in Si computed from molecular statics (MS) and from our framework. The first two columns show the formation energy in (eV). The last column shows the difference per atom between MS and Max-ent. Differences in formation energies are given in (meV).

	MS+$\frac{3N}{2}k_BT$	Max-ent	ΔE/atom
Vacancy defect ($N = 999$)	3.7181	3.6392	0.08
Tetrahedral interstitial ($N = 1001$)	4.3351	4.2807	0.055

4.1. Simulation setup

We consider Li nanopillars of circular cross section held at both ends by rigid platens, Fig. 3a. In this geometry, the nanopillars deform predominantly in plane strain and the calculations can be conveniently restricted to a slice of the nanopillar to a good approximation, Fig. 3b. Additionally, due to the large difference in the atomic size between Li and Si atoms, we assume that no substitutional alloying takes place upon lithiation and that the Li atoms occupy interstitial positions at all times. By this assumption, the Si sites are always fully occupied, i. e., $x_i = 1$ for all $i \in I_{\text{Si}}$, whereas the Li sites experience arbitrary degrees of occupation, $0 \leq x_i \leq 1$ for all $i \in I_{\text{Li}}$. For numerical stability reasons, we assume that the Li sites carry a minimum atomic molar fraction of 0.02, or 2%. This value of the atomic molar fraction cutoff is small enough that is causes a negligible perturbation of the initial conditions with respect to pristine Si. For instance, a uniform Li atomic molar fraction of 0.02 changes the equilibrium lattice parameter of Si from 5.43 Å to 5.58 Å.

The simulation cell consists of a slab of a diamond-Si nanopillar with diameter $D = 12$ nm and height $H = 2.7$ nm, Fig. 3b. The axis of the cylinder is aligned with the cube $\langle 001 \rangle$ direction of the diamond structure. The simulation cell contains a total of 14,465 Si sites and 72,545 interstitial sites. Periodic boundary conditions are enforced in the axis direction, while the lateral surface of the cylinder is set free. The adsorption process of Li into the nanopillar is of considerable interest in and of itself, but a detailed analysis thereof is outside the scope of the present work. Instead, we simply assume that the Si nanopillar is in contact with an environment characterized by an external chemical potential high enough as to result in full coverage, $x_i = 1$, over a surface layer of thickness $t = 0.2$ nm at all times during the charging process. All calculations are carried out at $T = 300$K.

We evolve the entire system in time, including both Si and Li sites, by

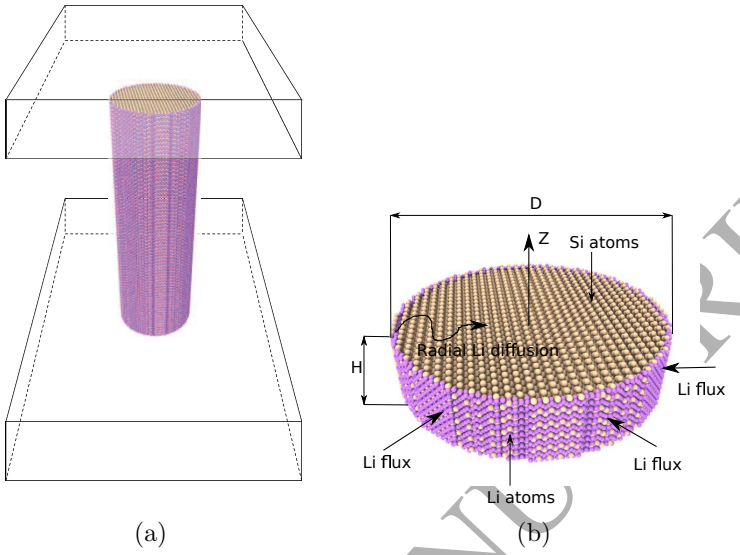

Figure 3: Computational model: (a) Si-based nanopillar; and (b) detail of a slab of the nanopillar.

means of a staggered scheme consisting of a forward integration of the atomic molar fractions at constant atomic positions followed by successive equilibrations of the system at constant atomic molar fractions, as summarized in Algorithm 1. During the equilibration step, we solve the system of coupled nonlinear equations (23a) and (23b) using a nonlinear GMRES solver in the PETSc library (Balay et al., 2016b,a, 1997), with the difference NGMRES-type option, two previous solutions and residuals (m=2) and the critical point option for the line search and $f_{tol} = 0.01eV/\text{Å}$. Further details of the NGMRES solver can be found in Oosterlee and Washio (2000) and Brune et al. (2015). At every equilibration step, all sites move until equilibrium of forces is attained. No restrictions are placed on the motion of the atoms, be they Si or Li. During the diffusion step, we integrate eq. (35) in time using a forward-Euler scheme with a diffusive cutoff radius of 3Å (Tritsaris et al., 2012; Dunst et al., 2015). We find that a time step of 0.38 milliseconds is sufficiently small to ensure numerical stability. We note that the equilibration and diffusion steps are coupled two ways: the mechanical forces on the sites depend on the atomic molar fractions and the driving forces for diffusion depend on the positions of the sites. In particular, energetically favorable Li

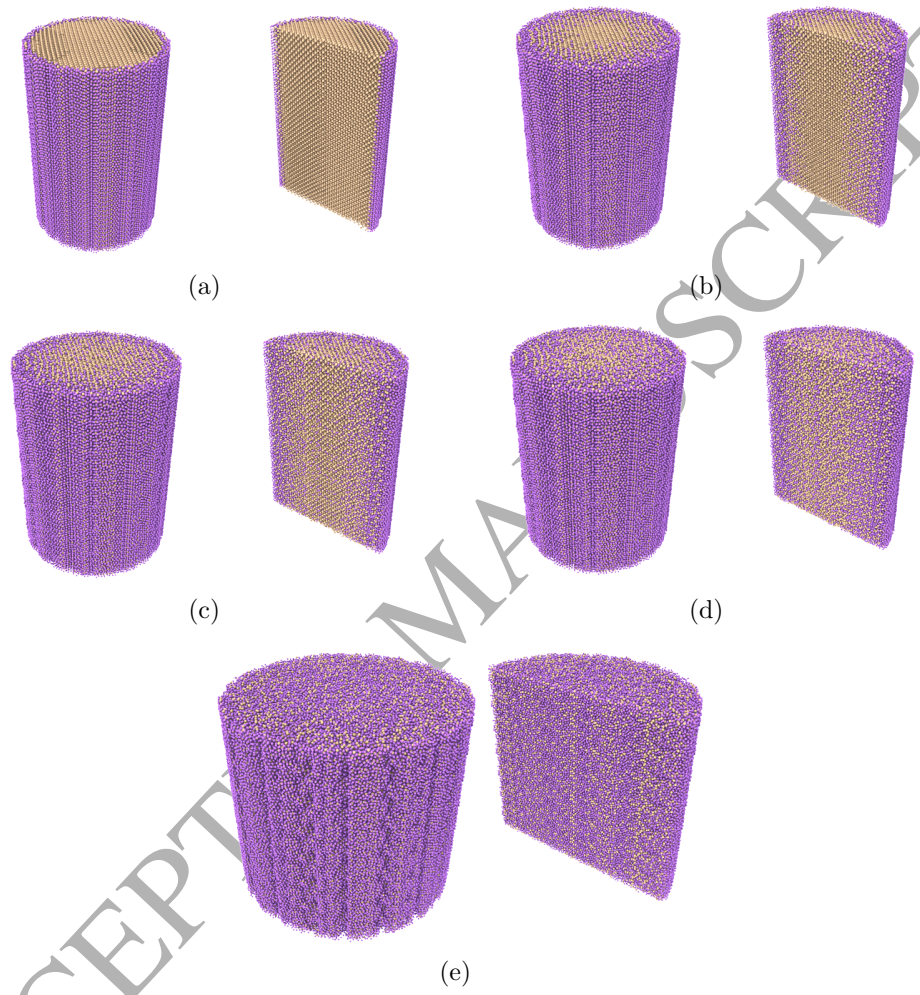

Figure 4: Snapshots of Si nanopillar lithiation: (a) t = 0.0 sec.; (b) t = 0.0008 sec.; (c) t = 0.005 sec.; (d) t = 0.01 sec.; and (e) t = 0.26 sec. Left side: perspective view of the full nanopillar; Right side: perspective view of the half nanopillar, as a result of a cut along the longitudinal axis. Li atoms are shown in violet color and Si atoms in beige color.

sites tend to be fully occupied at the expense of less energetically favorable sites. Following Obrovac and Christensen (2004) and Hatchard and Dahn (2004), the calculations are terminated when a level of lithiation of 3.75 Li atoms per Si is attained or, equivalently, when the ratio of total Li atoms and total Si atoms becomes 3.75. The simulation results are visualized using OVITO (Stukowski, 2010).

Algorithm 1 Diffusive Molecular Dynamics (DMD) algorithm

Input: $\{\bar{\boldsymbol{q}}^0\}$, $\{w^0\}$ and $\{x^0\}$
$n \leftarrow 0$
while total Li atoms/total Si atoms< max **do**
    Diffusive step: With $\{\bar{\boldsymbol{q}}^n\}$ and $\{w^n\}$ fixed,
    Get $\{x^{n+1}\}$ from (35) using forward-Euler.
    Equilibrium step: With $\{x^{n+1}\}$ fixed,
    Get $\{\bar{\boldsymbol{q}}^{n+1}\}$ and $\{w^{n+1}\}$ from (23a) and (23b) using NGMRES.
    Output: $\{\bar{\boldsymbol{q}}^{n+1}\}$, $\{w^{n+1}\}$ and $\{x^{n+1}\}$
    $n \leftarrow n + 1$

4.2. Silicon lithiation

The evolution of the nanopillar lithiation process over an elapsed time of 0.26 secs is shown in Fig. 4. Several periodic cells are combined in the time snapshots to aid visualization. The Li sites are decorated as violet and, for ease of visualization, their size is scaled according to their atomic molar fraction. For instance, a Li site with an atomic molar fraction $x_i = 0.5$ is half the size of a Li site with an atomic molar fraction $x_i = 1$. As may be seen from the snapshot sequence, Li gradually intercalates the Si nanopillar inward until an equilibrium steady state is reached consisting of a nearly uniform Li concentration. The evolution of the Li atomic molar fraction averaged over the circumferential direction is shown in Fig. 5 as a function of radial position. The transient profile evolves roughly in accordance with the diffusion equation. However, the fine structure of the evolution departs from classical diffusion due to the nonlinear dependence of diffusivity on the Li atomic molar fraction, the amorphization of Si (cf. Section 4.3) and the large volume expansion that accompanies lithiation (cf. Section 4.4). Previous work on lithium (Kim et al., 2014; Chon et al., 2011) and hydrogen (Wang et al., 2015; Sun et al., 2017) diffusion reveals that, in systems that undergo phase transitions, mass transport often occurs by the motion of

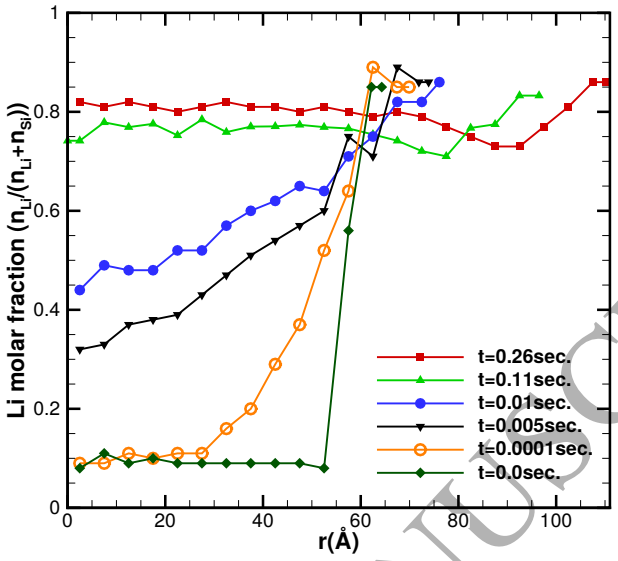

Figure 5: Li atomic molar fraction as a function of radius at different times. The total Li molar fraction for each time corresponds to 0.42, 0.97, 1.64, 1.99, 3.31 and 3.75, respectively.

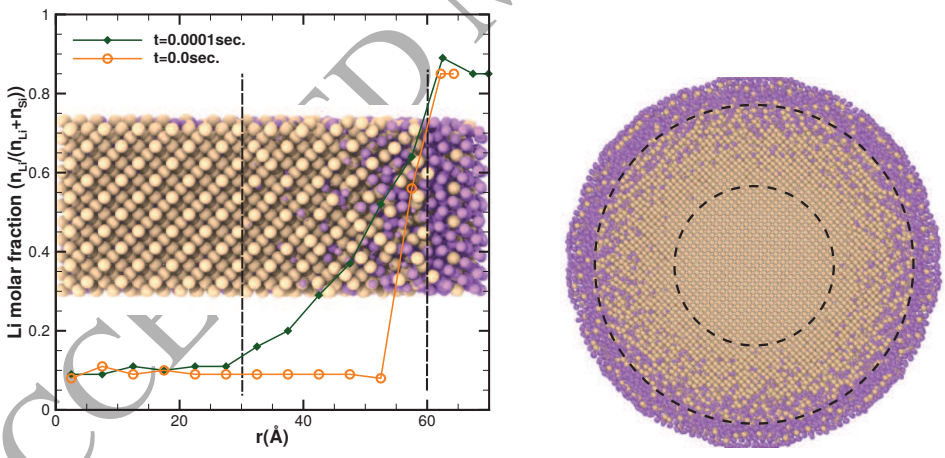

(a) (b)

Figure 6: (a) Li atomic molar fraction a function of radius at $t = 0.0001$ sec. Inset cross section shows the distribution of Li within the nanopillar. (b) Plan view of nanopillar with approximate location of the level contours $x_{\mathrm{Li}} = 0$ and $x_{\mathrm{Li}} = 1$ inscribed.

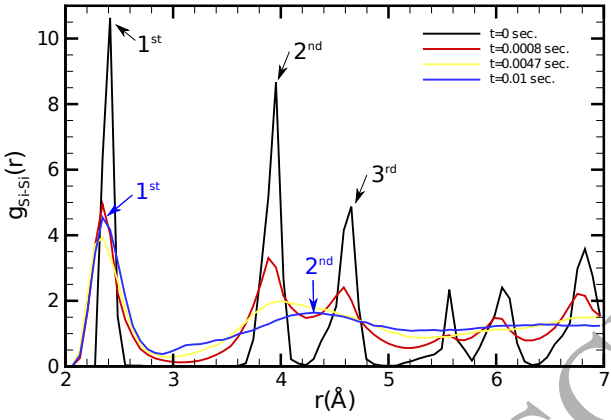

Figure 7: RDF for only Si atoms at different times before the full amorphization. The total Li molar fraction for each time corresponds to 0.42, 1.25, 1.64 and 1.99.

a relatively sharp phase boundary. In the Si-Li system, the thickness of the phase boundary is of the order of 30Å (Kim et al., 2014; Chon et al., 2011) and, thus, comparable to the size of the nanopillars, which prevents the formation of a sharp interphase. Indeed, after 0.0001s the calculated Li atomic molar fraction profile varies relatively smoothly across the nanopillar, Figs. 5 and 6. At 0.26 sec., we compute an average of Li atomic molar fraction of 0.79 and an average of local concentration of 0.006 Li atoms/Å^3. These results agree well with the values of 0.06 Li atoms/Å^3 and the ratio of 3.75 Li atoms per Si atom reported in Mohr et al. (2016) after lithiation, assuming a Si-atom density of 0.0474 Si atom/Å^3 and a volume expansion of 250-300%.

4.3. Silicon amorphization

Fig. 9 shows the evolution of the amorphization of Si during lithiation. The snapshots include the Si atoms only and the atoms are decorated according to their local crystal structure as determined from a common neighbor analysis (CNA) (Maras et al., 2016). The snapshot sequence reveals that amorphization starts at the outer boundary of the nanopillar and progresses inward. The CNA analysis suggests that amorphization involves intermediate structures. Full amorphization occurs rapidly, coming to completion in about 0.01 secs.

A quantitative characterization of the amorphization process may be based on a radial distribution function (RDF) analysis, which also provides

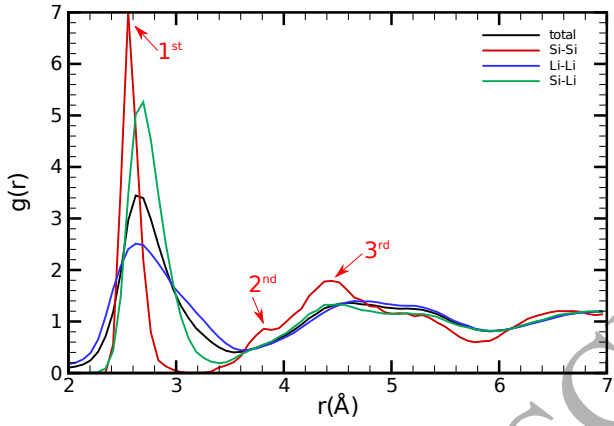

Figure 8: RDF for Si-Si, Li-Li and Si-Li after lithiation.

a basis for comparison with experimental data. The evolution of the RDF of the Si atoms is shown in Fig. 7. Initially, the RDF exhibits three first peaks at 2.35 Å, 3.84 Å and 4.50 Å, corresponding to the first, second and third nearest-neighbor distance, respectively, in the diamond structure. As lithiation progresses, these peaks decrease in amplitude and become broader. In the late stages of amorphization, the second and third peaks effectively disappear, signaling loss of crystallinity and decorrelation between Si atoms (Johari et al., 2011; Jung and Han, 2012; Ostadhossein et al., 2015). At $t = 0.01$ sec., only the first peak persists at 2.35 Å and a second new weak peak arises at 4.305 Å. The first peak results from short-order correlation between Si atoms through the formation of large numbers of dimers. The second peak is indicative of a weak long-order correlation between Si atoms. By way of comparison, Key et al. (2011) reported from an analysis of X-ray data that Si amorphization occurs once the third peak at $\approx$ 4.5 Å disappears, with a first broad peak remaining at 2.35 Å and a second weak peak appearing at 3.8 Å, in good agreement with our calculations.

After amorphization is complete, our calculations are suggestive of a certain degree of reconstruction resulting from the establishment of short-range Si-Li order. Fig. 8 shows the RDFs corresponding to Si-Si, Li-Li and Si-Li at full lithiation, $t = 0.26$ sec. Short-order peaks in the Si-Si, Li-Li and Si-Li RDFs at 2.55 Å, 2.63 Å and 2.7 Å, respectively, are evident in the figure. These values are roughly in keeping with fist peak values of 2.50 Å and 2.4 Å reported by Johari et al. (2011) and Jung and Han (2012), respectively.

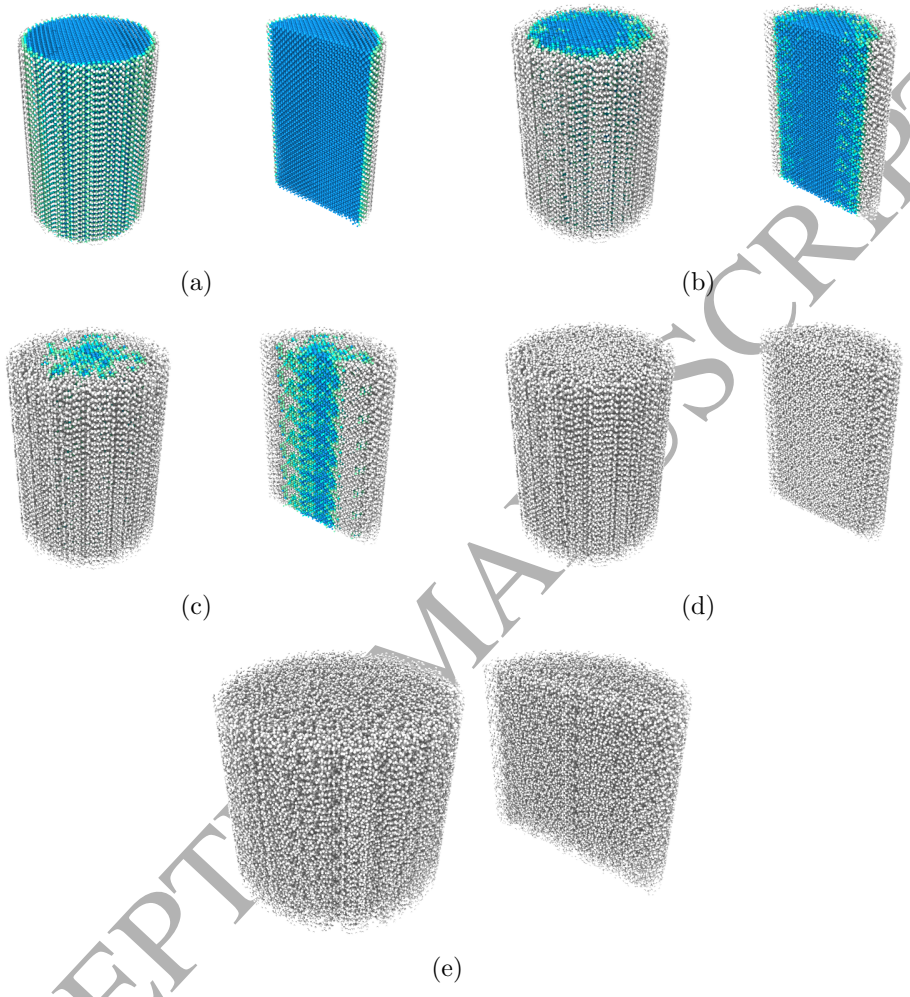

Figure 9: Amorphization of the Si nanopillar during the lithiation process (only Si atoms are shown): (a) t = 0.0 sec.; (b) t = 0.0008 sec.; (c) t = 0.005 sec.; (d) t = 0.01 sec.; and (e) t = 0.26 sec. Left: perspective view of the full nanopillar; Right: perspective view of half nanopillar. Local crystal structures are determined through a common neighbor analysis (CNA) (Maras et al., 2016). Blue color represents cubic diamond structure; Light blue represents cubic diamond structure (1st neighbor); Light green represents cubic diamond structure(2nd neighbor); and, white color represents other structure type.

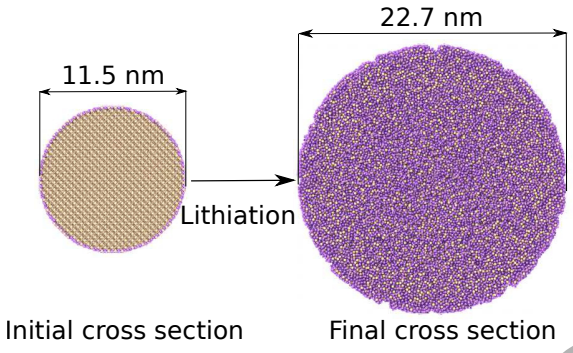

Figure 10: Detail of the diameter increase that takes place in Si-nanopillar after lithiation.

By contrast, Key et al. (2011) reported that after lithiation the first peak in the RDF shifts down to 2.27 Å. The shift of the Si-Si first peak up to 2.55 Å is indicative of a weakening of short-order Si-Si iterations. In addition, a new Si-Si peak appears at 3.82 Å while the second peak shifts to 4.42 Å from 4.305 Å. This weakening of short and long-range interactions at full lithiation may contribute to the large volume expansion attendant to amorphization.

4.4. Volume expansion

Our calculations predict a volume expansion of around 287% at full lithiation, which is in the ballpark of reported experimental values (Beaulieu et al., 2001, 2003). This extraordinary volume increase is illustrated in Fig. 10, which shows the cross section of the nanopillar before lithiation, with diameter $D \approx 11.5$ nm, and after lithiation, with diameter $D \approx 22.7$ nm.

The progression of the total volume of the nanopillar is shown in Fig. 11 as a function of the total Li molar fraction. By way of comparison, the figure also collects corresponding experimental measurements (Beaulieu et al., 2001, 2003) and previous computational results using molecular-dynamics calculations with the MEAM potential (Lee and Lee, 2014a) and *ab-initio* calculations (Johari et al., 2011). We note that these works are concerned with equilibrium properties corresponding to uniform Li concentrations, whereas our results are inhomogeneous and transient in nature. As may be seen from the figure, our calculations capture the general trends, especially when allowances are made for differences between the various works. The results show that the nanopillar expands slowly up to a total Li molar fraction of around 0.66, owing to the constraint on deformation exerted by the un-

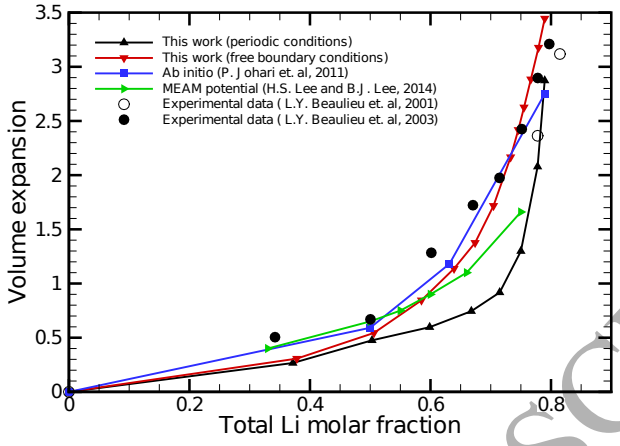

Figure 11: Comparison of the volume expansion versus the total Li molar fraction *vs.* experimental results (Beaulieu et al., 2001, 2003) and other calculations (Johari et al., 2011; Lee and Lee, 2014a).

lithiated core. The rate of expansion experiences a sharp increase once the nano-pillar is fully lithiated and that constraint is lost.

4.5. Volumetric strains

Owing to the transient and gradual progression of lithiation from the surface of the nanopillar inward, the volume change attendant to lithiation does not occur homogeneously within the cross section, which results in large misfit strains and residual stresses. Fig. 12 shows the evolution of the volumetric strain during lithiation. The strong transient inhomogeneity of the volumetric strain within the nanopillar is evident from the figure. Another noteworthy feature visible in Fig. 12 is a marked 'fraying-around-the-edges' at the boundary of the nanopillar. This fraying is suggestive of a complex process of volume expansion that is accompanied by deviatoric plastic flow. Under this scenario, when the first outer layer under the boundary of the nanopillar becomes lithiated and expands, it does so preferentially in the radial direction, a process that involves deviatoric plastic deformations in addition to volumetric change. We note that this process induces residual stresses of the order of the shear yield stress, which may be expected to be modest at best. When the next layer becomes lithiated, it pushes out the first layer causing it to develop large tensile hoop stresses and inducing fracture, or 'fraying', on radial planes.

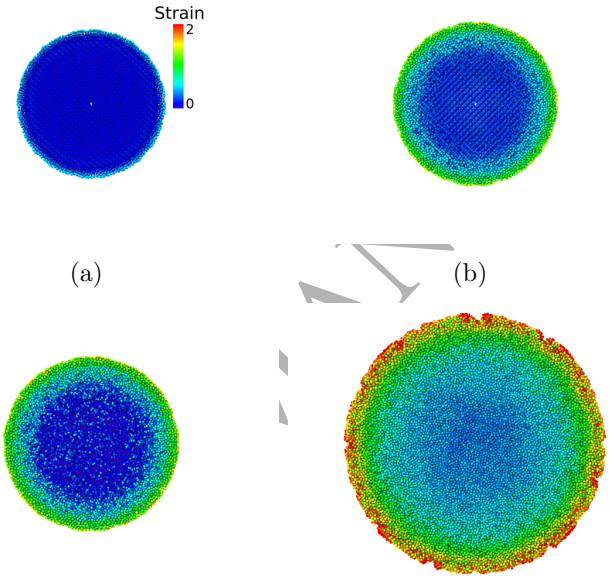

Figure 12: Volumetric strain of the nanopillar: (a) 0.0004 sec.; (b) 0.00082 sec.; (c) 0.01 sec.; and (d) 0.26 sec. The total Li molar fraction for each time corresponds to 0.42, 1.27, 1.99 and 3.75.

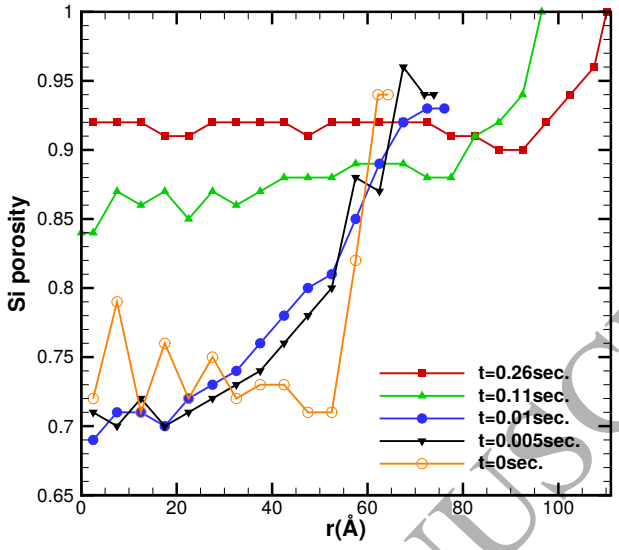

Figure 13: Evolution of the Si porosity, without considering the Li atoms, with respect to the radius of the nanopillar at different times. The total Li molar fraction for each time corresponds to 0.42, 1.64, 1.99, 3.31 and 3.75, respectively.

4.6. Porosity

The extent of structural damage and degradation induced by lithiation is closely correlated to the development of porosity, here identified with the free volume between the Si atoms. We have already noted that lithiation results in a shift in the Si-Si RDF first peak from 2.35 Å to 2.55 Å, indicative of a weakening of the Si-Si bonds and an increase in free volume, or porosity. This progress is clearly evident to visual inspection, e. g., in Fig. 9. However, the development of porosity occurs gradually and inhomogeneously during lithiation.

In order to track the fine structure of the porosity field and its evolution, we introduce the porosity measure

$$f_{Si}(r) = \frac{V_{total}(r) - V_{Si}(r)}{V_{total}(r)}, \tag{39}$$

where $V_{total}(r)$ is the volume of the annulus $\Omega(r) = (r - 2.5\text{Å}, r + 2.5\text{Å})$, $V_{Si}(r) = N_{Si}(r)\frac{4}{3}\pi r_{Si}^3$, $N_{Si}(r)$ is the number of Si atoms in $\Omega(r)$ and $r_{Si} = 1.11$ Å is the atomic radius of Si.

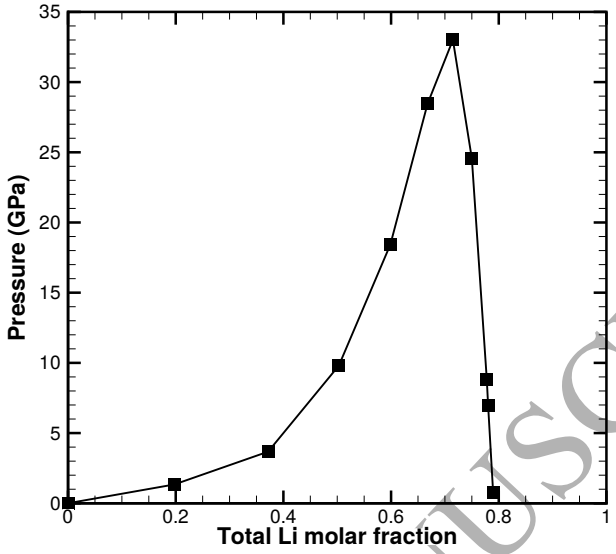

Figure 14: Evolution of the total average axial stress σ_{zz} *vs.* total Li molar fraction during the lithiation process.

Fig. 13 shows the evolution of $f_{Si}(r)$ during lithiation. As may be seen from the figure, porosity initially increases sharply under the surface of the nanopillar and then progresses towards its interior, roughly tracking the lithiation front. After the completion of lithiation, a nearly uniform distribution of porosity sets in in the interior of the nanopillar. This final core porosity is roughly 20% higher the initial porosity of Si. In addition, the final distribution of porosity exhibits a boundary layer of high porosity, or the order of 30% in excess of the initial porosity. This 'fraying-around-the-edges' effect is clearly visible in Fig. 9 and identifies the surface of the nanopillar as a likely site for spallation and structural failure.

The deleterious effect of porosity on the structural integrity of the nanopillar is illustrated in Fig. 14, which shows total average axial stress σ_{zz} *vs.* the total Li molar fraction during the lithiation process. As may be seen from the figure, the axial stress initial rises steeply with total Li molar fraction, reaching a peak in the vicinity of 35 GPa. Following that peak, the axial stress decays sharply with additional lithiation, a clear indication of a loss of bearing capacity of the material.

5. Concluding remarks

5.1. Summary and discussion

We have presented a fully-atomistic, physics-based, rigorously-derived method to simulate long-term mass-transport boundary-value problems on the diffusive time scale, thus greatly broadening the range and scope of problems that can be dealt with via atomistic models. Indeed, past capability has been limited to identifying diffusion pathways in very small samples, e. g., Tritsaris et al. (2012), or to inserting the Li atoms 'by hand' into the Si lattice, e. g., Lee and Lee (2014b). For instance, Lee and Lee (2014b) state about their calculations: *"It should be recalled that the purpose of the simulation is only to view what transpires as a result of the introduction of Li atoms in crystalline silicon at the initial stage of lithiation rather than to see the migration of the crystalline/amorphous interface, due to the time limitation of the molecular dynamics."* This disclaimer is, in fact, representative of the prior state of the art to this date.

The key enabling element of the present approach is a representation of mass transport through partial atomic molar fractions. In this representation, a collection of sites can be occupied by atoms of different species with variable probabilities. The atomic molar fractions evolve according to atomic-level kinetics, whereas the motion of the sites is governed by free-entropy maximization, with both processes coupled two ways. This representation eliminates the need to track individual atomic hops, thus making simulations on the diffusive time scale possible.

We have applied this novel methodology to the study of lithiation of Si nanowires. The simulations paint a picture of lithiation of Si nanowires as a conflation of complex and coupled phenomena with diffusive mass transport as the rate-controlling mechanism. The lithiation of Si alters radically its short range order as measured, e. g., by the radial distribution function, ultimately resulting in the amorphization of Si. In addition, lithiation induces extensive porosity in the Si lattice resulting in a severe degradation of its load bearing capacity. Finally, the transient nature of lithiation, which progresses largely by interfacial motion, and the attendant volume increase results in large misfit strains and residual stresses, some of them tensile and leading to surface cracks.

As noted at the introduction, poor structural reliability of Si nanowires, especially after repeated charge-discharge cycles, is a main impediment to their deployment in practical high-energy lithium-ion battery designs. A

number of nanostructured designs have been put forth for purposes of mitigating structural degradation in Si anodes, including hollow nanostructures and clamped hollow structures (Wu and Cui, 2012) and composite structures (Liu et al., 2017). Diffusive Molecular Dynamics provides an effective tool for assessing those and other design trade-offs with atomistic fidelity under realistic operating conditions.

5.2. Comparison with phase field methods

The similarities and differences between DMD and other methods bear careful discussion. For instance, the phase field crystal (PFC) method (cf., e. g., Baker and Curtin (2015) for a lucid critique) shares with DMD the ability to simulate slow and diffusive phenomena at the atomic scale by means of kinetic laws. However, DMD and PFC rest on very different physical foundations. Thus, PFC is based on a fundamental theorem of density functional theory (DFT) that states that the *equilibrium* Helmholtz free energy of a system of atoms is a unique functional of the *one-particle atomic density* $\rho^{(1)}(\boldsymbol{r})$. This renders PFC applicable—but also essentially limited—to the study of systems at chemical and thermal equilibrium. By contrast, our framework is based on fundamental principles of non-equilibrium statistical mechanics that provide a theoretical basis for the description of systems far from chemical and thermal equilibrium (Kulkarni, 2006; Venturini, 2011; Venturini et al., 2014).

The representational paradigms used in PFC and DMD are also radically different. As already noted, PFC describes the state of the system in terms of the one-particle probability density $\rho^{(1)}(\boldsymbol{r})$, which is a continuous function of position. A number of uncontrolled approximations result in a Helmholtz free energy that is expressed in terms of single and double integrals of $\rho^{(1)}(\boldsymbol{r})$. The computation of those integrals requires further approximations, typically based on the Fourier transform, and fitting of the kernels. Additional *ad hoc* terms are often added to the Helmholtz free energy in order to accomplish ancillary goals such as ensuring stability of vacancies and other structures. By way or sharp contrast, our DMD formulation is based on a straightforward representational paradigm that uses site coordinates and atomic molar fractions x_i. These atomic molar fractions arise from max-ent as the ensemble average, or 'convexification', of the instantaneous occupation numbers n_i of the sites.

The means by which PFC and DMD account for mass transport are likewise radically different. In PFC, diffusion is modelled through an *ad*

hoc linear kinetic law originating from the macroscopic phase field method and analogous to the heat equation. This kinetic equation involves a single scalar transport constant in the spirit of Fick's law of mass diffusion. We recall that the use of continuum parabolic differential equations to model diffusion in discrete systems is justified when the density gradients are small and smooth on the scale of the lattice, a situation rarely encountered at the nanoscale, especially in the presence of lattice defects. By contrast, our formulation of mass transport follows directly from Onsager's kinetic theory (Kulkarni, 2006; Venturini, 2011; Venturini et al., 2014) and simply expresses a general relation between atomic-level mass fluxes and chemical potentials. In the same manner as interatomic potentials need to be modeled, the kinetic relation is likewise subject to modeling. Previous work (Kulkarni, 2006; Kulkarni et al., 2008; Ariza et al., 2011; Ponga et al., 2015, 2016; Venturini, 2011; Venturini et al., 2014; Wang et al., 2015) has relied mostly on linear kinetics. In the present work, we follow Li et al. (2011) and resort to a *master equation* that computes effective transport rates using concepts from transition-state theory. The use of Onsager kinetics, in conjunction with appropriate master equations, enables the simulation of mass transport in systems far away from equilibrium in which the chemical potential gradients exhibit large atomic-level fluctuations, e. g., in the vicinity of lattice defects.

The main finding of Baker and Curtin (2015) is that, while PFC can adequately predict the Hemlzholtz free energy of complex systems with large lattice distortions, such as dislocation cores, it results in large errors when attempting to describe mass transport near lattice defects. This accuracy deficit owes mainly to the fact that the one-particle probability density is ill-defined for metastable configurations, leading to large errors in the sampling of the free energy and rendering PFC simulations only *qualitative*. Interestingly, Baker and Curtin (2015) suggest that these difficulties could be overcome, and PFC be made more quantitative, through the use of metastable free-energies in combination with master equations or by recourse to kinetic Monte Carlo schemes. The first approach is precisely that which is adopted in the present work.

5.3. Bayesian and frequentist interpretation of the results

Our approach is based on a Bayesian view of systems of particles, pioneered by Jaynes (Jaynes, 1957a,b), where all quantities of interest are computed as phase averages with respect to the *max-ent* probability density function of the system, which encodes the net sum of our *knowledge* of the state

of the system. From a frequentist point of view, the ensemble averages can be interpreted as empirical averages over multiple realizations—indeed, infinite realizations—of the same system. This paradigm shift between *frequentist to Bayesian* for purposes of modeling transport phenomena, including heat and mass diffusion, is a key distinction affording considerable competitive advantage to max-ent over other approaches, such as kinetic Monte Carlo, where configurations need to be sampled explicitly.

5.4. Accuracy and fidelity

Finally, we close this section with some comments on accuracy and fidelity. In the present approach, thermal effects, correlations and anharmonic effects are accounted for through phase-averaging with respect to the max-ent probability density function (7). Phase integrals are approximated using variational mean field theory. The accuracy of the mean field approximations can be controlled, in the sense of numerical convergence, e. g., by recourse to cluster expansions. In the calculations presented in this work, we specifically compute phase averages using third-order numerical quadrature and one-body mean field Hamiltonians. These approximations introduce local energy discrepancies of the order of 0.1 meV/atom with respect to MD values, cf. Section 3.4 on validation. This trade-off between accuracy and efficiency appears reasonable for the application at hand. However, should additional accuracy be needed, higher-order quadrature rules and mean field cluster expansions could be used in order to further control errors.

Acknowledgments

J. P. Mendez and M. Ortiz gratefully acknowledge support from the US National Science Foundation under award #1436950. M. Ponga gratefully acknowledges the support from the Natural Sciences and Engineering Research Council of Canada (NSERC) through the Discovery Grant under Award Application Number RGPIN-2016-06114 and the support of Compute Canada through the Westgrid consortium for giving access to the supercomputer grid. Sections 5.2, 5.3 and 5.4 were added to the paper during the review process at the request of reviewers.

References

Aifantis, K. E., Hackney, S. A., Kumar, R. V., 2010. High energy density lithium batteries: materials, engineering, applications. John Wiley & Sons.

Anderson, M. S., Swenson, C. A., Jan 1985. Experimental equations of state for cesium and lithium metals to 20 kbar and the high-pressure behavior of the alkali metals. Phys. Rev. B 31, 668–680.

Ariza, M. P., Romero, I., Ponga, M., Ortiz, M., 2011. Hotqc simulation of nanovoid growth under tension in copper. Int. J. Fracture 174 (1), 75–85.

Baker, K. L., Curtin, W. A., Jan 2015. Assessment of phase-field-crystal concepts using long-time molecular dynamics. Phys. Rev. B 91, 014103.

Balay, S., Abhyankar, S., Adams, M. F., Brown, J., Brune, P., Buschelman, K., Dalcin, L., Eijkhout, V., Gropp, W. D., Kaushik, D., Knepley, M. G., McInnes, L. C., Rupp, K., Smith, B. F., Zampini, S., Zhang, H., Zhang, H., 2016a. PETSc users manual. Tech. Rep. ANL-95/11 - Revision 3.7, Argonne National Laboratory.

Balay, S., Abhyankar, S., Adams, M. F., Brown, J., Brune, P., Buschelman, K., Dalcin, L., Eijkhout, V., Gropp, W. D., Kaushik, D., Knepley, M. G., McInnes, L. C., Rupp, K., Smith, B. F., Zampini, S., Zhang, H., Zhang, H., 2016b. PETSc Web page http://www.mcs.anl.gov/petsc.

Balay, S., Gropp, W. D., McInnes, L. C., Smith, B. F., 1997. Efficient management of parallelism in object oriented numerical software libraries. In: Arge, E., Bruaset, A. M., Langtangen, H. P. (Eds.), Modern Software Tools in Scientific Computing. Birkhäuser Press, pp. 163–202.

Beaulieu, L., Eberman, K., Turner, R., Krause, L., Dahn, J., 2001. Colossal reversible volume changes in lithium alloys. Electrochem. Solid St. 4 (9), A137–A140.

Beaulieu, L., Hatchard, T., Bonakdarpour, A., Fleischauer, M., Dahn, J., 2003. Reaction of li with alloy thin films studied by in situ afm. J. Electrochem. Soc. 150 (11), A1457–A1464.

Bower, A., Guduru, P., Sethuraman, V., 2011. A finite strain model of stress, diffusion, plastic flow, and electrochemical reactions in a lithium-ion half-cell. J. Mech. Phys. Solids 59 (4), 804 – 828.

Brune, P. R., Knepley, M. G., Smith, B. F., Tu, X., 2015. Composing scalable nonlinear algebraic solvers. SIAM Review 57 (4), 535–565.

Chan, C. K., Peng, H., Liu, G., McIlwrath, K., Zhang, X. F., Huggins, R. A., Cui, Y., 2008. High-performance lithium battery anodes using silicon nanowires. Nat. nanotechnol. 3 (1), 31–35.

Choi, N.-S., Yao, Y., Cui, Y., Cho, J., 2011. One dimensional si/sn-based nanowires and nanotubes for lithium-ion energy storage materials. J. Mater. Chem. 21 (27), 9825–9840.

Chon, M. J., Sethuraman, V. A., McCormick, A., Srinivasan, V., Guduru, P. R., Jul 2011. Real-time measurement of stress and damage evolution during initial lithiation of crystalline silicon. Phys. Rev. Lett. 107, 045503.

Cui, Z., Gao, F., Cui, Z., Qu, J., 2012a. A second nearest-neighbor embedded atom method interatomic potential for lisi alloys. J. Power Sources 207, 150 – 159.

Cui, Z., Gao, F., Qu, J., 2012b. A finite deformation stress-dependent chemical potential and its applications to lithium ion batteries. J. Mech. Phys. Solids 60, 1280–1295.

Deshpande, R., Cheng, Y.-T., Verbrugge, M. W., 2010. Modeling diffusion-induced stress in nanowire electrode structures. J. Power Sources 195 (15), 5081–5088.

Ding, N., Xu, J., Yao, Y., Wegner, G., Fang, X., Chen, C., Lieberwirth, I., 2009. Determination of the diffusion coefficient of lithium ions in nano-si. Solid State Ionics 180 (23), 222 – 225.

Dunst, A., Sternad, M., Epp, V., Wilkening, M., 2015. Fast li+ self-diffusion in amorphous lisi electrochemically prepared from semiconductor grade, monocrystalline silicon: Insights from spin-locking nuclear magnetic relaxometry. J. Phys. Chem. C 119 (22), 12183–12192.

Gonzalez-Ferreiro, B., Romero, I., Ortiz, M., 2016. A numerical method for the time coarsening of transport processes at the atomistic scale. Modelling and Simulation in Materials Science and Engineering 24 (4).

Haftbaradaran, H., Song, J., Curtin, W., Gao, H., 2011. Continuum and atomistic models of strongly coupled diffusion, stress, and solute concentration. Journal of Power Sources 196 (1), 361 – 370.
URL http://www.sciencedirect.com/science/article/pii/S0378775310010670

Hatchard, T. D., Dahn, J. R., 2004. In situ xrd and electrochemical study of the reaction of lithium with amorphous silicon. J. Electrochem. Soc. 151 (6), A838–A842.

Jaynes, E. T., May 1957a. Information theory and statistical mechanics. Phys. Rev. 106, 620–630.

Jaynes, E. T., Oct 1957b. Information theory and statistical mechanics. ii. Phys. Rev. 108, 171–190.

Johari, P., Qi, Y., Shenoy, V. B., 2011. The mixing mechanism during lithiation of si negative electrode in li-ion batteries: An ab initio molecular dynamics study. Nano Lett. 11 (12), 5494–5500.

Jung, S. C., Han, Y.-K., 2012. Ab initio molecular dynamics simulation of lithiation-induced phase-transition of crystalline silicon. Electrochim. Acta 62, 73–76.

Kasavajjula, U., Wang, C., Appleby, A. J., 2007. Nano-and bulk-silicon-based insertion anodes for lithium-ion secondary cells. J. Power Sources 163 (2), 1003–1039.

Key, B., Morcrette, M., Tarascon, J.-M., Grey, C. P., 2011. Pair distribution function analysis and solid state nmr studies of silicon electrodes for lithium ion batteries: Understanding the (de)lithiation mechanisms. J. Am. Chem. Soc. 133 (3), 503–512.

Kim, S.-P., Datta, D., Shenoy, V. B., 2014. Atomistic mechanisms of phase boundary evolution during initial lithiation of crystalline silicon. J. Phys. Chem. C 118 (31), 17247–17253.

Kuhn, A., Sreeraj, P., Pttgen, R., Wiemhfer, H.-D., Wilkening, M., Heitjans, P., 2011. Li ion diffusion in the anode material li12si7: Ultrafast quasi-1d diffusion and two distinct fast 3d jump processes separately revealed by 7li nmr relaxometry. J. Am. Chem. Soc. 133 (29), 11018–11021.

Kulkarni, Y., 2006. Coarse-graining of atomistic description at finite-temperature. Ph.D. thesis, Caltech.

Kulkarni, Y., Knap, J., Ortiz, M., 2008. A variational approach to coarse graining of equilibrium and non-equilibrium atomistic description at finite temperature. J.Mech. Phys. Solids 56 (4), 1417–1449.

Lee, B.-J., 2007. A modified embedded atom method interatomic potential for silicon. Calphad 31 (1), 95 – 104.

Lee, H.-S., Lee, B.-J., 2014a. Structural changes during lithiation and delithiation of si anodes in li-ion batteries: A large scale molecular dynamics study. Met. Mater. Int. 20 (6), 1003–1009.

Lee, H.-S., Lee, B.-J., 2014b. Structural changes during lithiation and delithiation of si anodes in li-ion batteries: A large scale molecular dynamics study. Met. Mater. Int. 20 (6), 1003 1009.

Lee, W.-C., Lee, S.-G., Chang, K. J., 1998. First-principles study of the self-interstitial diffusion mechanism in silicon. Journal of Physics: Condensed Matter 10 (5), 995.

Leung, W.-K., Needs, R. J., Rajagopal, G., Itoh, S., Ihara, S., Sep 1999. Calculations of silicon self-interstitial defects. Phys. Rev. Lett. 83, 2351–2354.

Li, J., Sarkar, S., Cox, W. T., Lenosky, T. J., Bitzek, E., Wang, Y., Aug 2011. Diffusive molecular dynamics and its application to nanoindentation and sintering. Phys. Rev. B 84, 054103.

Liu, Q., Cui, Z., Zou, R. J., Zhang, J. H., Xu, K. B., Hu, J. Q., 2017. Surface coating constraint induced anisotropic swelling of silicon in si-void@siox nanowire anode for lithium-ion batteries. Small 13 (13).

Magasinski, A., Dixon, P., Hertzberg, B., Kvit, A., Ayala, J., Yushin, G., 2010. High-performance lithium-ion anodes using a hierarchical bottom-up approach. Nat. Mater. 9 (4), 353–358.

Maras, E., Trushin, O., Stukowski, A., Ala-Nissila, T., Jnsson, H., 2016. Global transition path search for dislocation formation in ge on si(001). Comput. Phys. Commun. 205, 13 – 21.

Mohr, P. J., Newell, D. B., Taylor, B. N., 2016. Codata recommended values of the fundamental physical constants:2014. J. Phys. Chem. Ref. Data 45 (4), 043102.

Needs, R. J., 1999. First-principles calculations of self-interstitial defect structures and diffusion paths in silicon. Journal of Physics: Condensed Matter 11 (50), 10437.

Obrovac, M. N., Christensen, L., 2004. Structural changes in silicon anodes during lithium insertion/extraction. Electrochem. Solid-State Lett. 7 (5), A93–A96.

Oosterlee, C. W., Washio, T., 2000. Krylov subspace acceleration of nonlinear multigrid with application to recirculating flows. SIAM Journal on Scientific Computing 21 (5), 1670–1690.

Ostadhossein, A., Cubuk, E. D., Tritsaris, G. A., Kaxiras, E., Zhang, S., van Duin, A. C. T., 2015. Stress effects on the initial lithiation of crystalline silicon nanowires: reactive molecular dynamics simulations using reaxff. Phys. Chem. Chem. Phys. 17, 3832–3840.

Pichler, P., 2004. Intrinsic Point Defects, Impurities, and Their Diffusion in Silicon. Springer-Verlag Wien GmbH.

Plimpton, S., 1995. Fast parallel algorithms for short-range molecular dynamics. Journal of Computational Physics 117 (1), 1 – 19.

Ponga, M., Ortiz, M., Ariza, M. P., 2015. Finite-temperature non-equilibrium quasi-continuum analysis of nanovoid growth in copper at low and high strain rates. Mechanics of Materials 90, 253 – 267, proceedings of the IUTAM Symposium on Micromechanics of Defects in Solids.

Ponga, M., Ortiz, M., Ariza, M. P., 2017. A comparative study of nanovoid growth in fcc metals. Philosophical Magazine.

Ponga, M., Ramabathiran, A. A., Bhattacharya, K., Ortiz, M., 2016. Dynamic behavior of nano-voids in magnesium under hydrostatic tensile stress. Model. Simul. Mat. Sc. 24 (6), 065003.

Ruffo, R., Hong, S. S., Chan, C. K., Huggins, R. A., Cui, Y., 2009. Impedance analysis of silicon nanowire lithium ion battery anodes. J. Phys. Chem. C 113 (26), 11390–11398.

Ryu, I., Choi, J. W., Cui, Y., Nix, W. D., 2011. Size-dependent fracture of si nanowire battery anodes. J. Mech. Phys. Solids 59 (9), 1717–1730.

Sarkar, S., Li, J., Cox, W. T., Bitzek, E., Lenosky, T. J., Wang, Y., Jul 2012. Finding activation pathway of coupled displacive-diffusional defect processes in atomistics: Dislocation climb in fcc copper. Phys. Rev. B 86, 014115.

Sethuraman, V., Chon, M., Shimshak, M., Winkle, N. V., Guduru, P., 2010. In situ measurement of biaxial modulus of si anode for li-ion batteries. Electrochem. Commun. 12 (11), 1614 – 1617.

Simpson, G., Luskin, M., Srolovitz, D. J., 2016. A theoretical examination of diffusive molecular dynamics. SIAM Journal on Applied Mathematics 76 (6), 2175–2195.

Soni, S. K., Sheldon, B. W., Xiao, X., Bower, A. F., Verbrugge, M. W., 2012. Diffusion mediated lithiation stresses in si thin film electrodes. J. Electrochem. Soc. 159 (9), A1520–A1527.

Soni, S. K., Sheldon, B. W., Xiao, X., Tokranov, A., 2011. Thickness effects on the lithiation of amorphous silicon thin films. Scripta Mater. 64 (4), 307 – 310.

Stroud, A. H., 1971. Approximate calculation of multiple integrals. Prentice-Hall.

Stukowski, A., 2010. Visualization and analysis of atomistic simulation data with ovitothe open visualization tool. Model. Simul. Mater. Sc. 18 (1), 015012.

Sun, X., Ariza, M. P., Ortiz, M., Wang, K. G., 2017. Acceleration of diffusive molecular dynamics simulations through mean field approximation and subcycling time integration. Journal of Computational Physics 350, 470–492.

Touloukian, Y., Saxena, S., Hestermans, P., 1975. Thermophysical properties of matter-the tprc data series. volume 11. viscosity. Tech. rep., DTIC Document.

Tritsaris, G. A., Zhao, K., Okeke, O. U., Kaxiras, E., 2012. Diffusion of lithium in bulk amorphous silicon: A theoretical study. J. Phys. Chem. C 116 (42), 22212–22216.

Venturini, G., Wang, K., Romero, I., Ariza, M. P., Ortiz, M., 2014. Atomistic long-term simulation of heat and mass transport. J. Mech. Phys. Solids 73, 242 – 268.

Venturini, G. N., 2011. Topics in multiscale modeling of metals and metallic alloys. Ph.D. thesis, Caltech.

Wang, H., Ji, X., Chen, C., Xu, K., Miao, L., 2013. Lithium diffusion in silicon and induced structure disorder: A molecular dynamics study. AIP Advances 3 (11), 112102.

Wang, K. G., Ortiz, M., Ariza, M. P., 2015. Long-term atomistic simulation of hydrogen diffusion in metals. International Journal of Hydrogen Energy 40 (15), 5353–5358.

Wu, H., Cui, Y., 2012. Designing nanostructured si anodes for high energy lithium ion batteries. Nano Today 7 (5), 414–429.

Xiao, X., Liu, P., Verbrugge, M., Haftbaradaran, H., Gao, H., 2011. Improved cycling stability of silicon thin film electrodes through patterning for high energy density lithium batteries. J. Power Sources 196 (3), 1409 – 1416.

Xie, J., Imanishi, N., Zhang, T., Hirano, A., Takeda, Y., Yamamoto, O., 2010. Li-ion diffusion in amorphous si films prepared by {RF} magnetron sputtering: A comparison of using liquid and polymer electrolytes. Mater. Chem. Phys. 120 (23), 421 – 425.

Yan, X., Gouissem, A., Sharma, P., 2015. Atomistic insights into li-ion diffusion in amorphous silicon. Mech. Mat. 91, Part 2, 306 – 312, mechanics of energy conversion and storage.

Yao, Y., McDowell, M. T., Ryu, I., Wu, H., Liu, N., Hu, L., Nix, W. D., Cui, Y., 2011. Interconnected silicon hollow nanospheres for lithium-ion battery anodes with long cycle life. Nano lett. 11 (7), 2949–2954.

Yeomans, J. M., 1992. Statistical mechanics of phase transitions. Oxford University Press.

Yim, W. M., Paff, R. J., 1974. Thermal expansion of aln, sapphire, and silicon. J. Appl. Phys. 45 (3), 1456–1457.

Yoshimura, K., Suzuki, J., Sekine, K., Takamura, T., 2007. Measurement of the diffusion rate of li in silicon by the use of bipolar cells. J. Power Sources 174 (2), 653 – 657, 13th International Meeting on Lithium Batteries.

Zhang, F., Curtin, W. A., 2008. Atomistically informed solute drag in almg. Model. Simul. Mat. Sc. 16 (5), 055006.

Zhao, K., Wang, W. L., Gregoire, J., Pharr, M., Suo, Z., Vlassak, J. J., Kaxiras, E., 2011. Lithium-assisted plastic deformation of silicon electrodes in lithium-ion batteries: a first-principles theoretical study. Nano Lett. 11 (7), 2962–2967.